International Journal of
MATERIALS RESEARCH

Zeitschrift für METALLKUNDE

Original Contributions

S. Lingala[a], D. Jayne[b], F. Ernst[a]
[a] Department of Materials Science and Engineering, Case Western Reserve University, Cleveland, Ohio, USA
[b] The Lubrizol Corporation, Wickliffe, Ohio, USA

Effect of lubricant additives on the tribological behavior of aluminum alloy against steel

This study aims to understand the impact of various lubricant additives on the friction- and wear behavior of aluminum alloys against steel. Employing the aluminum alloy Al 6061 and the steel AISI E 52100 as representatives, we studied the effects of the main additives typically found in fully formulated lubricants individually by formulating model lubricants consisting of base oil and just one additive at a time. The additives we studied include sulfurized olefin, complex alkyl phosphate amine, alkyl phosphite, overbased calcium sulphonate, zinc dithiophosphate (ZDP), and calcium sulfonate detergents. For each model lubricant, as well as for the base oil and the fully formulated oil, we performed ball-on-disc experiments with aluminum alloy balls on steel discs. We obtained the friction coefficient, determined the wear volume of the aluminum alloy, and analyzed the composition of the wear surface. We found that all additives except calcium sulfonate detergents promote the formation of aluminum oxide. Among all individually tested additives, zinc dithiophosphate provides the best wear resistance, while sulfurized olefin provides the lowest friction. The lowest friction combined with the second lowest wear rate was actually observed for a fully formulated oil (containing an optimized mixture of several additives).

Keywords: Tribology; Aluminum–steel; Lubricants; Additives

1. Introduction

More than ever before, automobile manufacturers are trying to develop fuel-efficient and highly durable internal combustion engines. An important contribution to this desirable development are lighter engines enabled by high-strength Al-base (aluminum-base) alloys with good corrosion resistance, high fatigue strength, and low coefficients of thermal expansion [1, 2].

Under these criteria, Al–Si alloys have recently been considered as one of the best candidate alloys for pistons and cylinders, while a hard steel serves as piston-ring material. For this combination of materials, however, optimal lubricants still need to be developed. Cases of engine failure due to excessive wear as well as the energy dissipation caused by the piston-rings sliding against cylinders have stimulated research on the wear behavior of Al-base alloys against steel. Important research has been carried out on this tribopair under dry-sliding conditions (e. g. [3–5]). The general tribological behavior of steel has also been studied with a wide range of lubricants and lubricant additives (e. g. [6–8]). Still at the beginning are studies aiming to develop an understanding of the sliding behavior of Al-base alloys against steel in the presence of different lubricants and lubricant additives [3, 9–17]. A systematic overview of additives is provided by Spikes [18]. Jimenz et al. and Carol et al. have carried out profound microcharacterization of Al–Si alloys slid over AISI 52100 steel in the presence of ZDDP (alkyl zinc dithiophosphate) and MoDTC (molybdenum dithiocarbamate) lubricants. They concluded that combining ZDDP with MoDTC provides better wear resistance compared to ZDDP alone because combining the two addi-

tives enables the formation of a stable tribo-film [19–21]. De Barros Bouchet et al. discovered that adding fatty amine to ZDDP and Mo-based additives can further reduce friction and wear [22]. Chen et al. [20] studied the Al–Si and steel tribo-pair in the presence of different oils (mineral oil, polyalphaolefin, monoester, polyester, polyalkalyne glycol) with ZDDP, sulfur-, and phosphorus-containing additives, each individually added to these oils. Mineral oil showed better wear performance over the other oils and mineral oil with ZDDP showed a great improvement in friction and wear performance over the lubricant containing only sulfur- and phosphorus-providing additives alone. This work emphasized TEM (transmission electron microscopy) characterization of the tribo-film along with surface characterization through XPS (X-ray photoelectron spectrometry). Pereira [19, 23] investigated the chemical and mechanical properties of tribo-films formed by sliding an Al–Si alloy (A383) against E52100 steel in fully formulated oils. The results showed very low wear on the Al–Si alloy in fully formulated oil compared to oil with only ZDDP. This contrasts with the wear on the E52100 steel, which was higher in fully formulated oil than in oil with ZDDP alone.

To date, most of the work carried out on tribo-pairs of Al–Si alloys and steel has been on analyzing friction, wear, and tribo-layer formation of counteracting surfaces in rather complex lubricants – consisting of base oil and a variety of different additives. Most of these studies have not attempted to isolate the effects of individual additives and how they contribute to the overall performance of fully formulated lubricants. However, understanding the individual roles of different additives is of great importance for understanding the complex reactions that take place at tribo-surfaces and to recognize principles that may enable the engineering of better lubricants. The present study constitutes an attempt to isolate and understand the effects of the individual additives that are found in a typical "fully formulated" oil for lubricating Al-base alloys sliding against steel. For this purpose, and in order to understand how the effects of individual additives superimpose with each other in a fully formulated lubricant, we performed comparative wear tests in just the base oil, in lubricants consisting of base oil and just one additive, and in fully formulated oil. The aluminum alloy (Al 6061) we selected for this study is considered as an alternative to the presently used Al–Si alloys, which are harder, but more difficult to lubricate reliably. The results of our study provide important insights for the design of effective lubricants.

2. Experimental

Friction and wear testing was performed with Al 6061 balls and AISI E 52100 steel discs in a CETR ball-on-disc-type tribometer. The Vickers hardnesses of the steel and the aluminum alloy are 850 and 110, respectively. In accordance with ASTM (American Society for Testing and Materials) Standard G99-05 [24], as described e. g. by Wan and Xue [25], the ball and the disc were completely immersed in lubricant (liquid). In these tests, we set the normal load, sliding velocity, lubricant, temperature, and time to 2.4 N, 0.8 m s^{-1}, 50 ml, 353 K (80°C), and 1.8ks (30 min). The kinetic coefficient of friction μ_k was obtained from the applied normal force F_n and the friction force F_f indicated by the sensors of the tribometer according to

$$\mu_k \equiv \frac{F_f}{F_n} \tag{1}$$

Plotting μ_k as a function of time t yielded the "friction profile" of the respective tribo-system. The steady-state μ_k was obtained by averaging the data over the last 700 s of the friction curve.

To measure the dimensions of the scar that evolved on the ball, each ball was optically imaged and topographically scanned by LSCM (laser scanning confocal microscopy) in a BX62 FV1000 (Olympus) instrument [26].

The volume V_w the ball lost by wear was determined from the measured diameter d_s of the wear scar according to [12]

$$V_w = \frac{1}{3}\pi h^2(3R_0 - h) \tag{2}$$

and

$$h = R_0 - \sqrt{R_0^2 - \frac{d_s^2}{4}} \tag{3}$$

where R_0 denotes the ball radius and h the wear depth. These expressions assume that the wear scar is flat, a reasonable assumption under the conditions of our experiments: (i) No pile up of material was observed when viewed under a confocal microscope even before cleaning surface. Apparently, the piled-up material must have been taken up by the lubricant. (ii) The asperities (peaks and valleys) in the worn surface) did not exhibit height differences (from peak to valley) that we could measure with our equipment, and our attempts to capture plowed material were not successful at this small wear volume loss.

The chemical composition of the worn surfaces was analyzed by AES (Auger electron spectrometry), using a PHI-680 scanning Auger microprobe system (Perkin-Elmer).

The chemical compositions of the as-received materials were analyzed by XEDS (X-ray energy-dispersive spectrometry) in a Quanta 3D environmental dual-beam FIB (focused ion beam) system. Table 1 shows the results. The Al

Table 1. Composition of Al 6061 and AISI E 52100.

Material	Element/Atom Fraction (%)					
AISI E 52100	Fe 96.00 ± 0.50	Si 0.50 ± 0.05	Cr 1.60 ± 0.08	Mn 0.40 ± 0.05	P 0.10 ± 0.03	Total 100
Al 6061	Mg 1.00 ± 0.16	Al 94.70 ± 0.72	Cu 1.20 ± 0.02	Zn 2.70 ± 0.45	Si 0.00 ± 0.00	Total 100

6061 balls ("spherical pins" in the terms of the ASTM standard) had a diameter of 6 mm. The AISI E 52100 discs had a thickness of 6 mm and a diameter of 70 mm. The average surface roughness of both the balls and the discs was $R_a = 0.2$ μm.

The ball-on-disc wear tests were carried out with lubricants consisting of pure base oil, base oil with individual additives, and fully formulated oil. Table 2 itemizes these lubricants, details their compositions, and introduces short names to which we refer in the following.

Every experiment was repeated three times and the results were found to be consistent.

2.1. Transmission electron microscopy

In order to prepare specimens for TEM, we utilized a Quanta 3D environmental dual-beam system (FEI), providing a scanning electron beam and a (scanning) FIB. Two TEM samples were prepared from the Al alloy wear scar with dimensions $10 \times 8 \times 0.1$ μm^3, using a lift-out technique and deposition on ultra-thin amorphous carbon support films on Cu grids. One sample, TEM-P, was prepared by choosing an area of 2.5×2.5 μm^2 on the wear scar parallel to the sliding direction (Fig. 1). The other sample, TEM-V was prepared with its plane vertical to the sliding direction. The motivation for this approach was that AES maps from the Al surface exposed to L7-FFO showed dominance of different elements in alternative wear tracks on the wear scar. Therefore, preparing samples exclusively parallel to the sliding direction may have produced non-representative results.

The TEM samples were studied in a 200 kV LIBRA 200FE (Zeiss) and a 300 kV Tecnai F30ST (FEI). Selected-area diffraction patterns and bright-field- and dark-field images were recorded to understand the crystal structure and morphology of the tribo-film. Further, we performed dark-field "Z-contrast" STEM (scanning transmission electron microscopy) imaging using a HAADF (high-angle annular dark-field) detector (Fischione). Compositional analysis was carried out by XEDS with an Si–Li detector (129 eV energy resolution, Tracor Northern) and EELS (electron energy-loss spectrometry) using a GIF (Gatan Imaging Filter) equipped with a 2k × 2k CCD (charge-coupled device) camera.

Table 2. Lubricant Compositions.

Name	Description
L1-MBO	Group II mineral base oil.
L2-SOf	L1-MBO with 0.2 mass% sulfurized olefin, providing a high activity of sulfur – suitable for chemically reacting with a metal surface to form metal sulfides.
L3-APa	L1-MBO with 0.5 mass% complex alkyl phosphate amine, providing a high activity of phosphorus – suitable for chemically reacting with a metal surface to form metal phosphides.
L4-APi	L1-MBO with 0.50 mass% alkyl phosphite, providing a lower activity of phosphorus than phosphates do.
L5-OCS	L1-MBO with 0.7 mass% overbased Ca sulphonate detergent.
L6-ZDP	L1-MBO with 0.5 mass% secondary zinc dithiophosphate.
L7-FFO	Fully formulated oil API SN 5W-30.

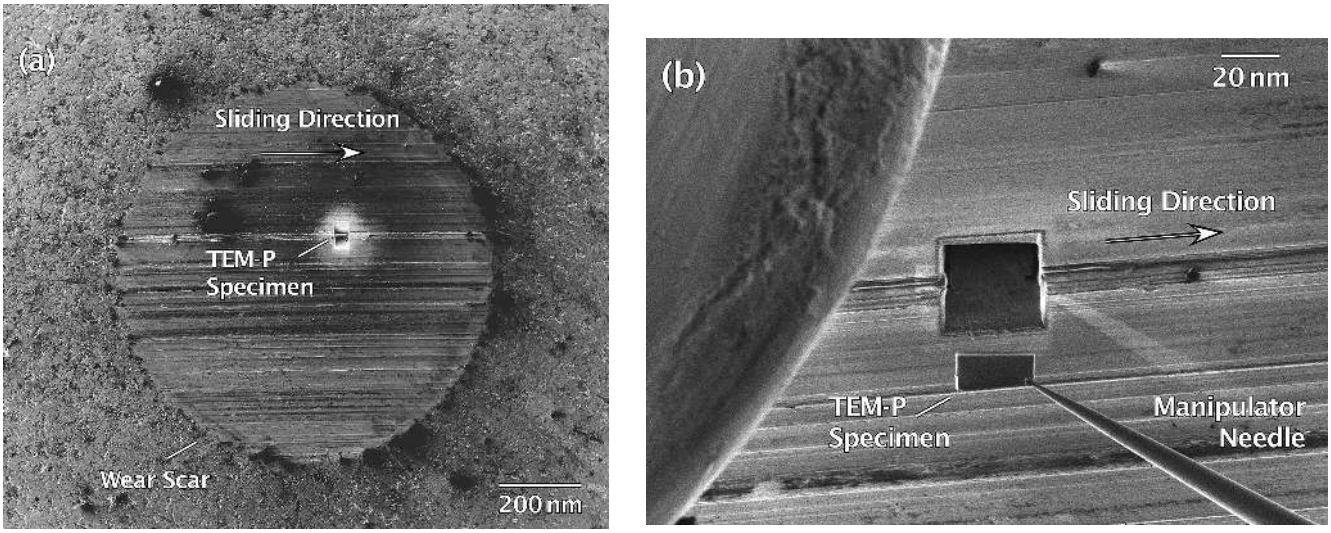

Fig. 1. Preparation of specimen TEM-P. (a) SEM SE (secondary electron) image of the wear scar and the trenches cut by FIB, leaving a vertical slab parallel to the sliding direction, which will become specimen TEM-P. (b) SEM secondary-electron image of the lift-out process of TEM-P, the sample prepared parallel to the sliding direction.

3. Results

3.1. Friction coefficients

Figure 2 shows the friction trace $\mu[t]$, i.e. the friction coefficient as a function of sliding time for three different experimental conditions: dry sliding, lubrication by base oil, and lubrication by a lubricant with additive. Accordingly, the specimens that were tested in the presence of lubricants reached steady-state conditions after 0.1 ks, i.e. 6 % of the test duration. For dry sliding conditions, however, steady-state conditions were only obtained after about one third of the test duration. Figure 3 displays the steady-state friction coefficients measured between Al 6061 and AISI E 52100 in the presence of the individual lubricants of Table 2. The error limits for these data are ±0.0001. The lowest friction coefficient (0.024) is observed for L7-FFO, closely followed by L2-SOf (0.042). Among the phosphorus-containing lubricants, L3-APa shows the lowest friction coefficient (0.074), nearly double the value observed for L2-SOf. The friction coefficients observed for L6-ZDP, L5-OCS, and L4-APi are significantly higher – actually somewhat higher than that of pure base oil, L1-MBO (0.088).

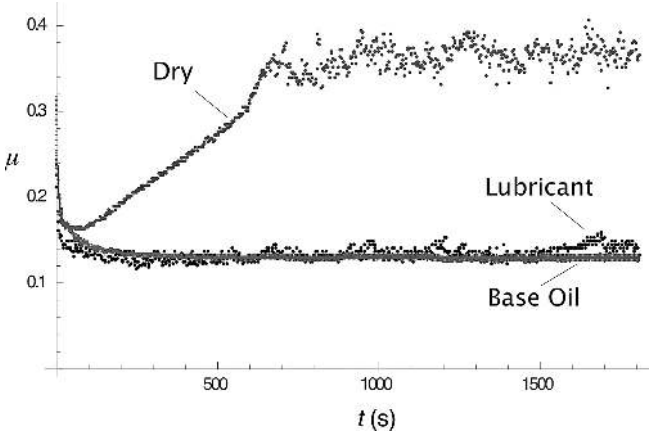

Fig. 2. Friction trace $\mu[t]$, i.e. friction coefficient as a function of time for three different experimental conditions: dry sliding, lubrication by base oil, and lubrication by a lubricant with additive.

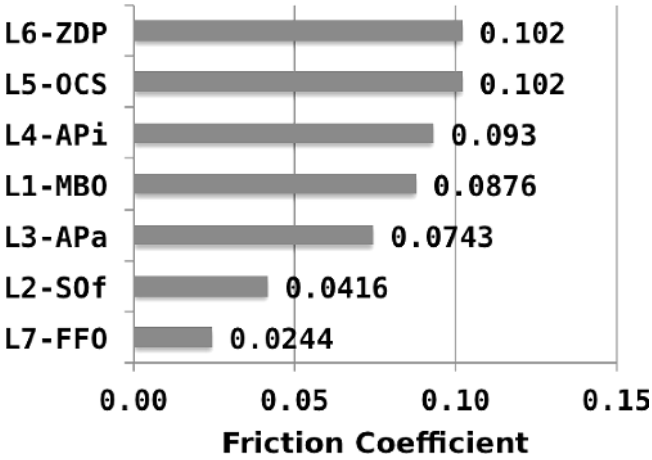

Fig. 3. Steady-state coefficient of friction measured for the individual lubricants of Table 2.

3.2. Wear volume loss on Al balls

Figure 4 presents a tableau showing the LSCM images of the wear scars on the Al 6061 balls after wear tests with the lubricants listed in Table 2. Figure 5 shows the wear volume loss for each specimen, obtained via Eq. (2) from the measured wear scar diameters d_s indicated in Fig. 4. All lubricant additions improve the performance of L1-

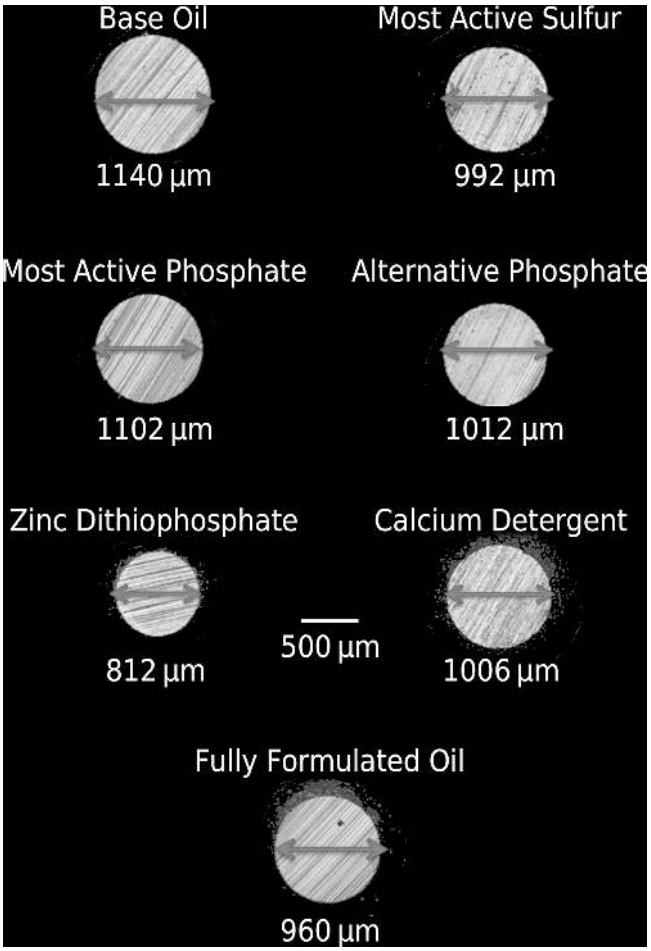

Fig. 4. Wear scars observed by LSCM after wear testing dry and with lubricants containing different additives.

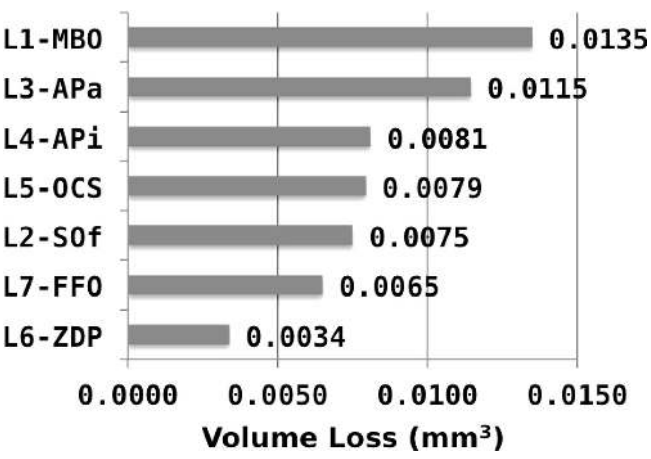

Fig. 5. Volume loss of the Al 6061 ball due to wear for the individual lubricants of Table 2.

MBO. The lowest volume loss (0.0034 mm^3) is observed for L6-ZDP, implying that under the applied conditions, pure base oil with the sole addition of ZDP (zinc dithiophosphate) provides better wear resistance than any other lubricant considered here – including the "fully formulated oil," L7-FFO. L7-FFO actually provided the second-best wear resistance, although the volume loss (0.0065 mm^3) is nearly twice as high as for L6-ZDP. L2-SOf, L4-APi, and L5-OCS produced similar volume losses, all of them slightly higher than that of L7-FFO. The worst volume loss – apart from L1-MBO (0.014 mm^3) – was observed for L3-APa (0.012 mm^3).

4. Surface–lubricant interactions

Friction and wear sensitively depend on the physical and chemical interactions between the lubricant and the surfaces of the tribo-pair. In order to investigate what chemical reactions take place on the Al 6061 side during wear testing with each lubricant in Table 2, we obtained composition–depth profiles from the wear scars of the Al 6061 balls with the help of a SAM (scanning Auger microprobe). First, we observed the SEM (scanning electron microscopy) image of the Al 6061 wear scar. An example is shown in Fig. 6. Then, alternating Ar (argon) sputtering and compositional analysis by AES were carried over a field of about 25 μm^2 and to a depth of at least 100 nm in each case. The composition–depth profiles obtained for the individual lubricants of Table 2 are shown in Figs. 7 to 12. All composition–depth profiles feature a spike of carbon at the surface and a constant carbon signal of about 10 at.% at depths below $\approx$10 nm. These omnipresent features suggest that the carbon signal mainly originates from carbon contamination of the specimen surface with adventitious carbon (from the rest gas of the instrument vacuum), rather than interaction of the Al 6061 surface with the individual lubricants.

Figure 7 presents the composition–depth profile for L2-SOf. A constant and very low sulfur signal indicates that Al 6061 is not reacting with sulfur species in the lubricant. However, the strong oxygen signal from the surface into a depth of about 80 nm indicates that L2-SOf oxidizes Al 6061 during the wear test and the oxide is kneaded into the alloy. This hypothesis is confirmed by TEM studies [27].

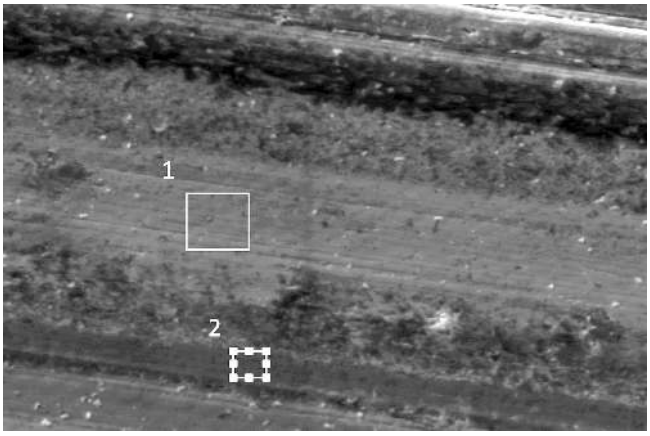

Fig. 6. Scanning electron microscopy image showing the wear scar of an Al 6061 ball after wear testing in lubricant L7-FFO.

Figures 8 and 9 show the composition–depth profiles after wear testing in L3-APa and L4-APi. These data reveal no chemical reactions involving phosphorus; the phosphorus signal is very low and constant in both cases. The interactions between the surfaces and the active-phosphor-containing lubricants mainly generates an oxygen-rich layer – likely consisting mainly of Al_2O_3 (as this is the most stable oxide) – with a depth of $\approx$50 nm. Apparently, Al 6061 is oxidized even in the presence of APa (complex alkyl phosphate amine)- and APi (alkyl phosphite)-containing lubricants.

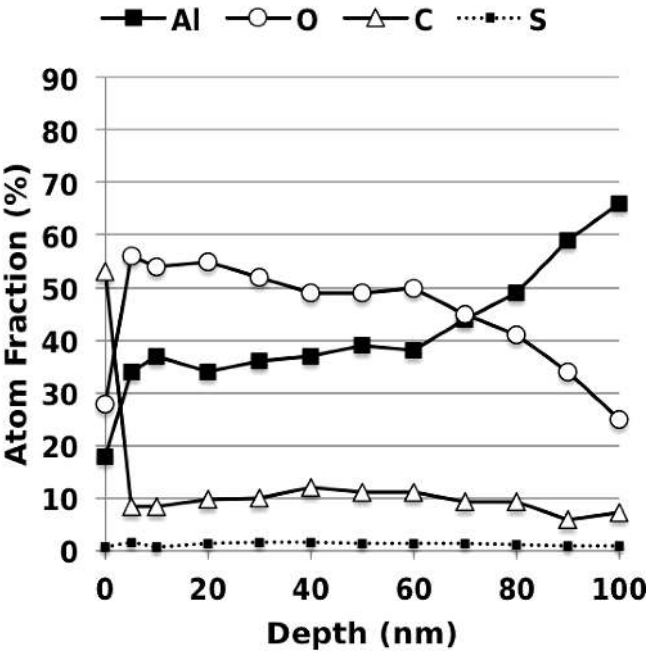

Fig. 7. Elemental fraction–depth profiles measured for the Al 6061 ball after wear testing in lubricant L2-SOf.

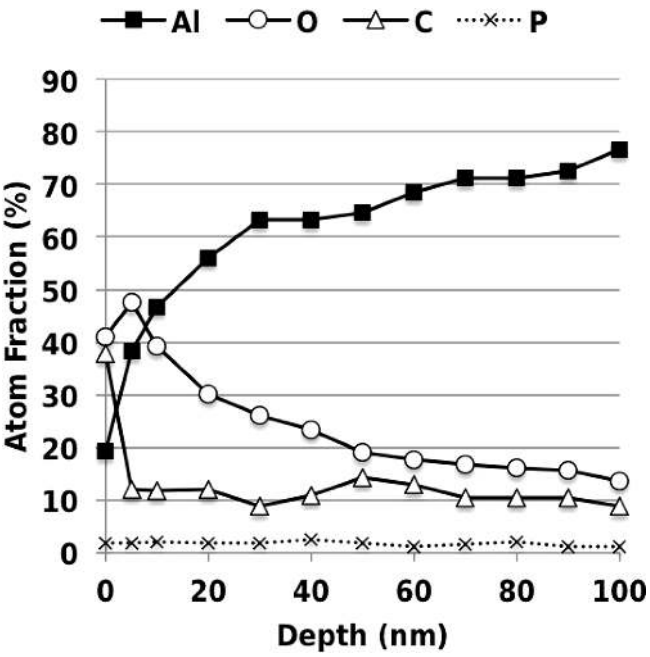

Fig. 8. Elemental fraction–depth profiles measured for the Al 6061 ball after wear testing in lubricant L3-APa.

Figure 10, the composition–depth profile of Al 6061 after wear testing in L6-ZDP, indicates hardly any wear-induced chemical interaction of Zn, sulfur, and phosphorus with the Al 6061 surface. Only within the first 5 nm of depth, the profile shows significant Zn and sulfur signals. At larger depths than that, the signals of these two elements are constant and below the detection limit of our instrument, as is the signal of phosphorus over the entire range of sampled depth. The only significant change in composition is observed with regard to oxygen. Within the first 40 nm, the concentration of oxygen is higher than that of Al. In the vicinity of depth $z \approx 10$ nm, the oxygen-to-Al atom fraction ratio roughly corresponds to Al_2O_3, suggesting that a significant volume fraction of this oxide has formed. As an Al_2O_3 layer with much smaller thickness usually passivates the surface of Al-base alloys, the observed oxygen-rich layer suggests that the oxide forms at the surface and is kneaded into the alloy by plastic flow during the wear test.

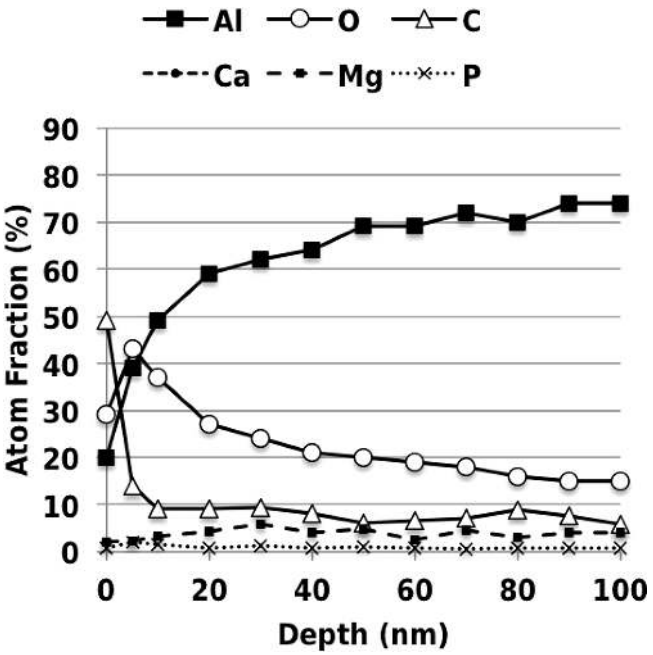

Fig. 9. Elemental fraction–depth profiles measured for the Al 6061 ball after wear testing in lubricant L4-APi.

Figure 11 indicates that wear testing in L5-OCS causes a strong reaction of the worn Al 6061 surface with Ca and O. Within the first ≈ 20 nm below the surface, the wear scar mainly consists of Ca and oxygen with an atom fraction ratio of 2 : 1. With increasing depth, the fraction of Al increases as the fraction of Ca decreases. The oxygen fraction remains constant over the entire depth interval from 0 to 100 nm. Apparently, this surface layer consists of a mixture of CaO and Al_2O_3. The inset at the top-right of Fig. 11 shows the same concentration–depth profiles for Al, oxygen, and Ca as the main graph, but down to 80 nm below the surface. Accordingly, significant concentrations of Ca penetrate into depths of at least 70 nm. Ca and oxygen actually dominate (over Al) from the surface down to ≈ 15 nm.

Figure 6 presents an SEM image of the Al 6061 ball wear scar after testing in L7-FFO, the fully formulated oil. Since in this case the SEM image suggests that different regions may have different compositions, composition–depth analysis was carried out twice – in Region 1 and Region 2 marked in Fig. 6.

Figure 12 shows the result obtained from Region 1, while Fig. 13 shows the result obtained from Region 2. Both data sets suggest that the topmost ≈ 10 nm of the wear scar consist of an oxygen-and Al- rich layer with a composition approximately corresponding to Al_2O_3. With increasing depth, the Al signal increases, while the oxygen signal decays in both cases. While these main features are similar in

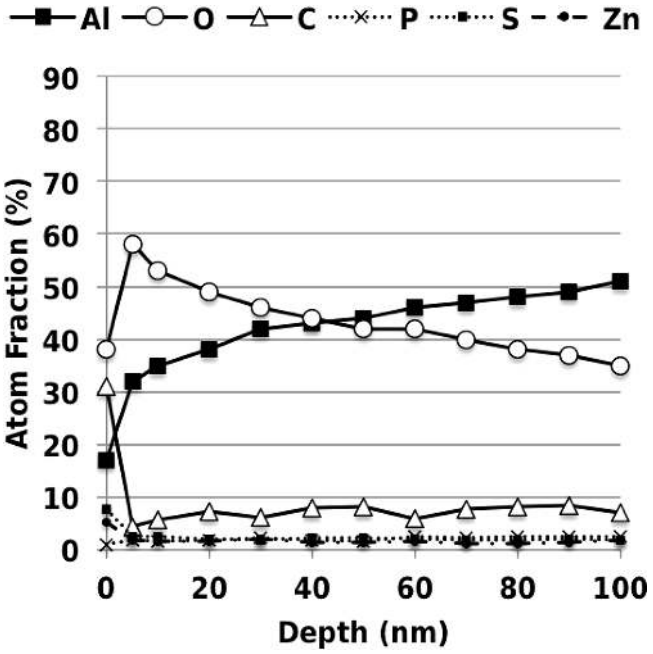

Fig. 10. Elemental fraction–depth profiles measured for the Al 6061 ball after wear testing in lubricant L6-ZDP.

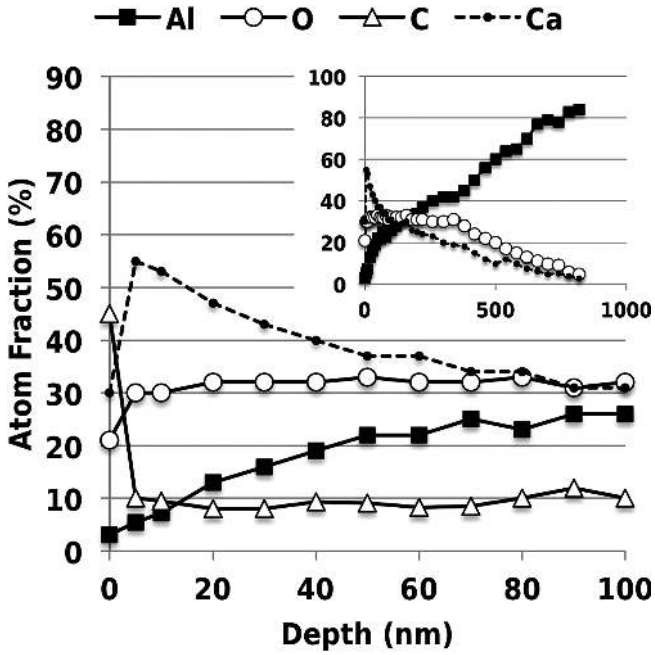

Fig. 11. Elemental fraction–depth profiles measured for the Al 6061 ball after wear testing in lubricant L5-OCS.

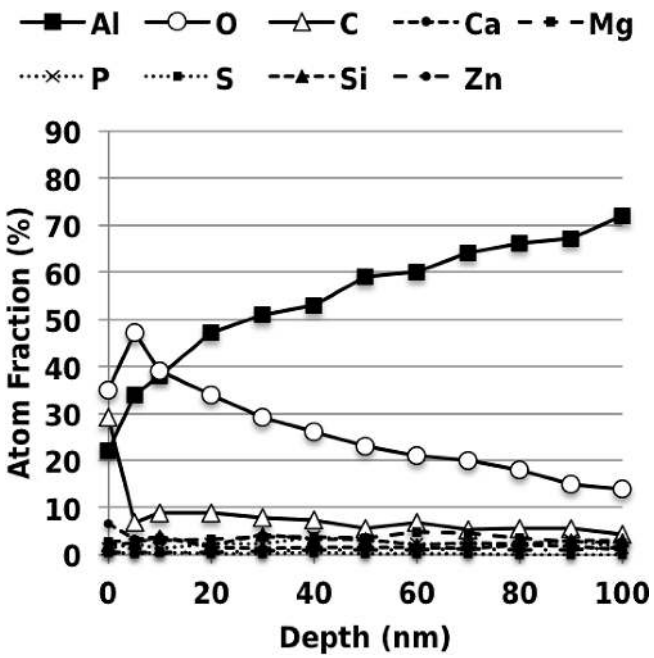

Fig. 12. Elemental fraction–depth profiles measured for the Al 6061 ball in region 1 of Fig. 6 after wear testing in lubricant L7-FFO.

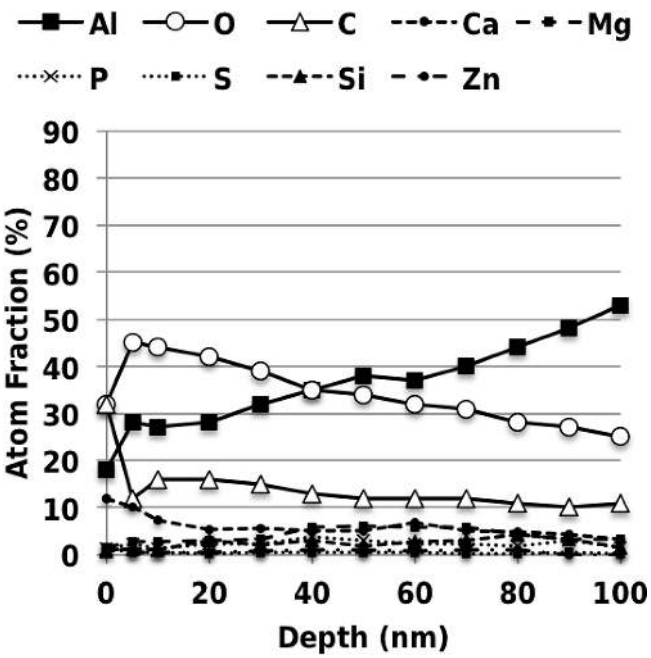

Fig. 13. Elemental fraction–depth profiles measured for the Al 6061 ball in region 2 of Fig. 6 after wear testing in lubricant L7-FFO.

the two regions marked in Fig. 6, they do significantly differ in the depth below which the Al fraction is higher than the oxygen fraction. While the cross-over point of the Al- and the oxygen graph is a depth of only 10 nm in Region 1, oxygen dominates down to $\approx$40 nm in Region 2. Also, the slope of the Al- and oxygen graphs is smaller in Fig. 13 than in Fig. 12, confirming that Region 2 was penetrated by oxygen to greater depth than Region 1. Apart from the omnipresent carbon, the concentration of the other elements is rather small in both regions. The only notable exception is Ca. The data from both regions marked in Fig. 6 indicate an enhanced concentration of Ca of up to about 10 at.% near the surface. Within the first $\approx$5 nm of depth, the Ca fraction decreases to a few atomic percent and remains at this level down to a depth of 100 nm in both data sets.

Figure 14 presents Auger electron intensity maps from a wear scar region of the Al 6061 specimen tested in L7-FFO. The maps were obtained by SAM for each relevant element after first sputtering 5 nm off the wear scar surface. The image at the top was recorded with a secondary electron detector, i.e. represents an SEM image showing surface topography. The brightness and contrast of the individual maps in Fig. 14 have been adjusted to reveal details of the intensity distribution. For this and for other reasons, the relative abundance of the individual elements cannot be inferred by comparing intensities between corresponding maps. However, the intensity variations observed in each map do correctly represent corresponding local variations of the near-surface concentration of the respective elements.

Interestingly, the spatial distribution of all elements that produced sufficient signal-to-noise ratios – i.e. all elements except for Fe (iron) and phosphorus – correlates with the surface topography revealed by the SEM image. The Al map and the oxygen map resemble the SEM image, whereas the carbon-, Ca (calcium)-, sulfur-, and Zn (zinc) map resemble a *negative* of the SEM image. This indicates that the ridges on the wear scar are rich in Al and oxygen, whereas the valleys are rich in carbon, Ca, sulfur, and Zn.

5. Microcharacterization

The aim of our microcharacterization work was to understand how the microstructure of the Al alloy evolves under the wear scar. Figure 15a presents a Z-contrast STEM image of TEM-P, prepared with its plane *parallel* to the sliding direction from the Al alloy tested with L7-FFO. Within a 3 μm deep zone below the surface, the image features diffuse, wiggly bright contours approximately parallel to the surface. Apparently, these lines are artifacts of non-uniform FIB milling (thickness variations). Within a 0.3 μm deep zone directly below the surface, a different morphology is observed. The magnified STEM micrograph of this region in Fig. 15b reveals small grains elongated in the *sliding* direction parallel to the surface. Their short axes are typically 0.1 μm and their long axes typically several 0.1 μm, i.e. significantly smaller than the average grain size in the as-received alloy, which is in the range of several 1 μm. No tribo-film is observed in these images.

Figure 15c shows a corresponding Z-contrast STEM image for TEM-V, prepared with its plane normal to the sliding direction. Figure 15c exhibits microstructural contrast patterns different from those in Fig. 15a. No "wiggling" contours appear within the 3 μm deep zone. Again, a different grain morphology is observed within a 0.3 μm deep zone directly below the surface. In this case, however, the small grains appear more equi-axed than elongated, with a typical diameter of 0.1 μm. Figure 15d presents a highly magnified BF (bright-field) image featuring a (rotated) selected region of Fig. 15c. In a half-lens-shaped grain at the surface, this image also reveals small particles with dia-

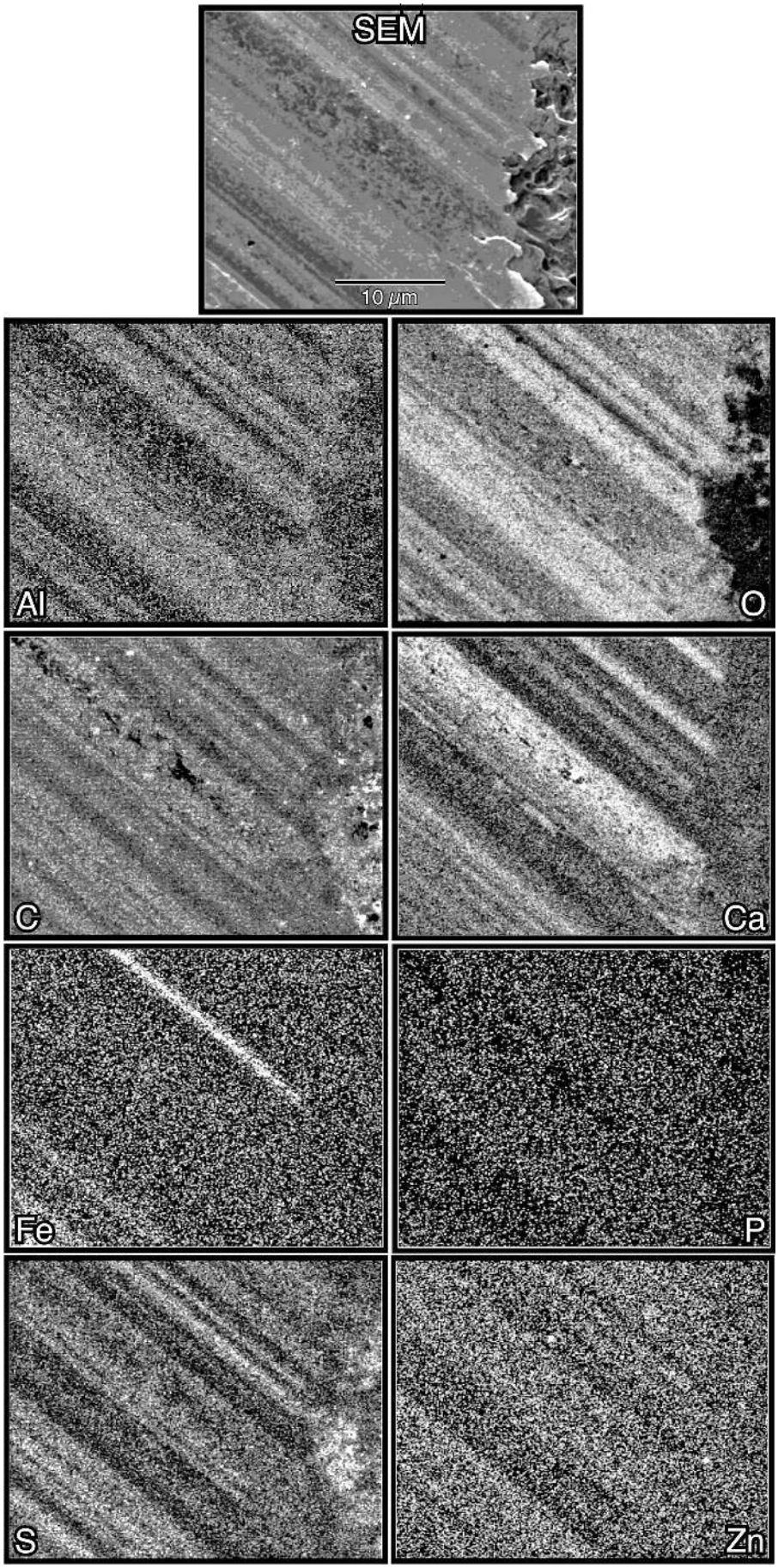

Fig. 14. Montage of an SEM image and AES elemental maps from the wear scar of the Al 6061 ball after wear testing in lubricant L7-FFO.

meters of order 10 nm. Presumably these are strengthening Mg_2Si precipitates that are already present in the as-received Al 6061.

5.1. X-Ray energy-dispersive spectrometry

In Fig. 15, we have identified three microstructure components of interest for compositional analysis: (1) dark regions, (2) bright regions, (3) bright contours. For TEM-V, the markers in Fig. 15c and d indicate locations from which we acquired XEDS spectra. Arrows point at locations of spot analysis, from which we obtained spectra with a resting electron-beam with a spot size of about 10 nm in diameter (at the specimen surface). Boxes indicate rectangular regions over which an electron beam with the same diameter was scanned during the analysis. The results are shown in Table 3 (Series A, Fig. 15c) and Table 4 (Series B, Fig. 15c). The elemental compositions at the individual locations, obtained after background subtraction and Cliff–Lorimer k-factor correction, are indicated in terms of atom fractions. For the data in Table 3, we estimate error limits of ±5 %for oxygen and ±0.5 % for Al, Si, Ca, Cr, Fe, Cu. For the data in Table 4, we estimate error limits of ±5 % for oxygen and ±0.5 % for Al, Mg, Ca, Cr, Fe, sulfur, and phosphorus.

In the following, we exclude Cu signals from the discussion as they originate from the specimen holder of the transmission electron microscope.

For Series A, the locations indicated in Fig. 15c, XEDS analysis indicated the following: In Region A1, the presence of mainly Fe, Si and Cr is observed, along with a low level of Al. The bright regions in which markers A1 and A2 are placed in Fig. 15c can be envisioned as material transferred from the steel counterpart through the Al alloy

Table 3. Atom Fractions by XEDS – Series A.

Loc	O-K	Al-K	Si-K	Ca-K	Cr-K	Fe-K	Cu-K
A1	10	66	5	0	3	8	7
A2	6	67	2	0	2	10	10
A3	58	4	0	25	0	0	12
A4	8	63	0	0	0	0	28
A5	5	89	0	0	0	0	4
A6	8	6	0	0	0	0	84

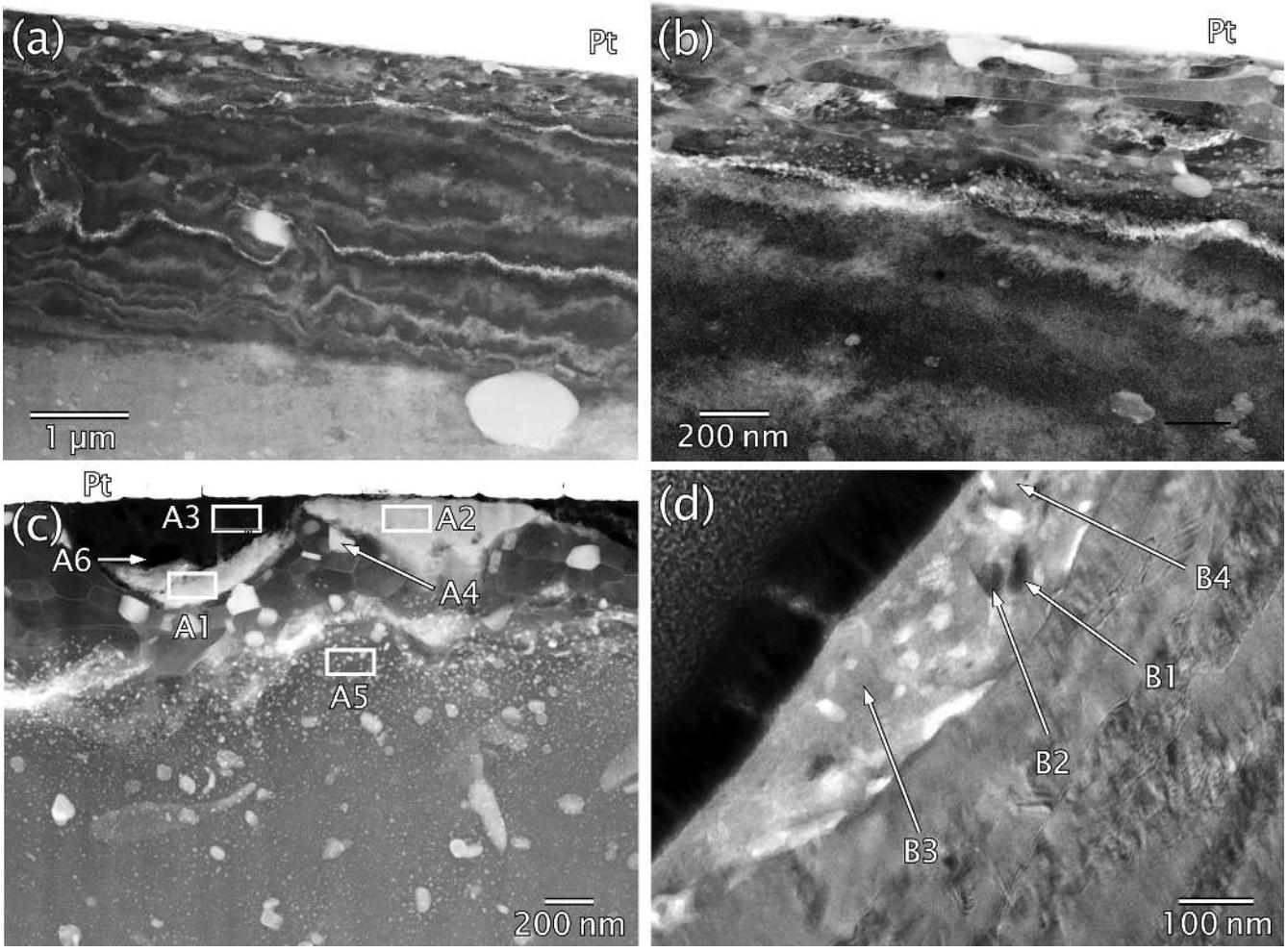

Fig. 15. Cross-sectional TEM images of the Al 6061 after testing with lubricant L7-FFO. "Pt" indicates the protecting platinum layer used in FIB preparation. The markup indicates regions from which we have obtained XEDS spectra for compositional analysis. (a) TEM-P. Z-contrast image at low magnification. (b) Magnified region of Fig. 15a. (c) TEM-V. Z-contrast image at medium magnification. (d) Conventional TEM BF image of the dark region around marker P3 in Fig. 15c. The rotation of this image versus Fig. 15c is caused by the characteristics of electromagnetic lenses.

surface into the Al alloy. Region A1 is 0.2 µm below the surface. This can be understood by assuming that this region has formed in the early stages of sliding and was then pushed deeper into the Al alloy by additional material deposited on the surface.

The XEDS spectrum of Region A3, which appears dark in Fig. 15c, features strong contributions from Ca and oxygen. Strong signals from Cu and Al are observed in Region A4. Region A5 shows mainly Al element, which surprises as fine particles are observed in the Z-contrast image of Fig. 15c in addition to the Al matrix. The spectrum from Region A6 only shows strong peaks of Cu, presumably from the Cu grid supporting the specimen. Apparently, some of the dark regions in the Z-contrast image are voids that may have formed during sliding.

For Series B, the following observations were made by XEDS analysis of the locations indicated in Fig. 15d: Region B1 is mainly composed of Fe and Cr, although Ca, Al, and oxygen are also detected. Region B2 produced significant signals from Ca, P, and oxygen. Region B3 is rich in Ca, oxygen, and Mg. Region B4 is rich in Ca and oxygen, but also contains moderate fractions of Fe, Cr, and phosphorus. These results indicate that material from the steel disc has been incorporated into the Al alloy. The bright grey matrix in Fig. 15d, which appears dark in the Z-contrast image of Fig. 15c, is mainly composed of Ca and oxygen, although it also contains Fe, Cr, and phosphorus.

Accordingly, the regions that appeared dark in Z-contrast constitute a film formed due to the reaction of the lubricant with the interacting surfaces during sliding. This film can be called a "tribo-film."

5.2. Selected-area diffraction

To study the crystal structure of the Ca–oxygen tribo-film, we recorded SAD (selected-area diffraction) patterns in relevant specimen regions. Figure 16 presents an example. The ring pattern in Fig. 16b indicates that the small grains are not strongly textured (in the sense of preferred crystal lattice orientation). As demonstrated by the markup in the figure, the ring pattern is consistent with the hypothesis that the majority of those grains are CaO with the rocksalt structure. The innermost reflections may originate from another oxide with a larger unit cell. The dark-field image in Fig. 16c was obtained by placing a small objective aperture onto the pair of innermost rings of the CaO structure. Accordingly, the grains that light up bright in this image are (some of the) CaO grains. Their size varies between $\approx$1 nm and 0.1 µm. Summarizing, the tribo-film mainly consists of CaO crystallites whether diameter of order $\approx$10 nm.

6. Discussion

In the following, we compare and discuss the observations made for the different lubricants. As we intended to simulate application-relevant scenarios, the mass fractions of the additives were not the same in each case. While it may be argued that this may impact the results, for each additive all relevant molecular species were sufficiently abundant at the metal surfaces to ensure that if a chemical reaction was thermodynamically favorable, we would have detected the products.

Table 4. Atom Fractions by XEDS – Series B.

Loc	O-K	Mg-K	Al-K	P-K	S-K	Ca-K	Cr-K	Fe-K
B1	26	0	5	0	0	7	5	56
B2	65	0	3	25	0	7	0	0
B3	51	13	7	1	1	27	0	1
B4	53	0	14	2	1	30	0	1

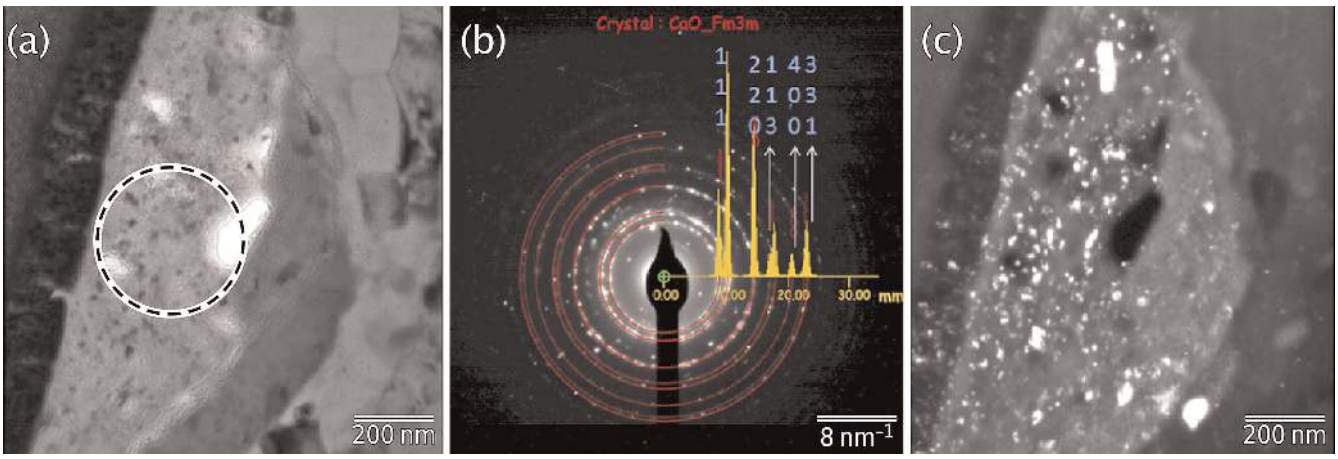

Fig. 16. SAD study of the tribo-film on Al 6061 after testing with L7-FFO. (a) Z-contrast STEM image showing the region of interest. The circular marker indicates the position of the area-selecting aperture when the diffraction pattern was recorded. (b) SAD pattern recorded from the region indicated in Fig. 16a. The ring pattern and relative intensities were obtained by a simulation assuming the rocksalt crystal structure of CaO. (c) DF (dark-field) image obtained by placing a circular objective aperture onto a section of the two innermost rings of Fig. 16a.

6.1. Lubricant with active sulfur

L2-SOf contains a sulfurized olefin. When added to a lubricant, thermal decomposition of the olefin during service releases active (elemental) sulfur [28], which can react with the sliding surfaces. The literature suggests that for steel-on-steel tribo-pairs, a reaction with sulfur provides a lubrication effect by formation of FeS on both surfaces [28]. This model is supported by the fact that FeS is mechanically soft. For tribo-pairs of steel with Al-base alloys, it is understood that owing to differences in formation enthalpy in the relevant temperature range between 300 and 700 K (100 to 400 °C), FeS forms much more readily than AlS. When the formation of sulfide (FeS) in the lubricant begins to decrease the sulfur activity, the lubricant becomes oxidized through free-radical chain reactions involving oxygen dissolved in the lubricant and/or from the ambient. This, in turn, promotes oxidation of Al at the Al 6061 surface, as observed in the composition–depth profiles. The product, Al_2O_3, is much harder (Mohs hardness: 9) than that of FeS (Mohs hardness: 4) [28]. Therefore, the formation of Al_2O_3 on the Al 6061 surface can reduce the wear rate of the Al 6061 alloy by preventing direct contact and adhesion of elemental Al to the steel surface [28].

6.2. Lubricants with active phosphorus

In general, phosphorus-containing compounds are considered as extreme-pressure and anti-wear additives to lubricants. The interaction of phosphorus with the Al 6061-AISI E 52100 tribo-pair can be explained by the following mechanism [25, 29]: (i) The combined action of applied mechanical shear stress and elevated temperature breaks chemical bonds of phosphorus in the molecules of the phosphorus-containing additive. This process, called "tribo-fragmentation", results in the formation of highly reactive molecular fragments. (ii) Molecule fragments react with the metal surfaces to form phosphate-rich films. (iii) As the temperature reaches the critical range for transition from low to high wear regime, the phosphate gets increasingly replaced by oxide.

Our observations are consistent with this model. However, we observed higher friction and lower wear for L4-APi than for L3-APa. The reason seems to be that phosphites (L4-APi) generally have a lower TRA (temperature of reaction activation) than phosphates (L3-APa). Therefore, phosphites react more readily with AISI E 52100 and Al 6061.

In the literature [25], the phosphate ($FePO_4$ or $Fe_3(PO_4)_2$) film forming on steel is observed to have low shear strength. It has been proposed that phosphorus also reacts with Al to form $AlPO_4$. Presumably, $AlPO_4$ is also mechanically weak. Accordingly, the phosphate layer will be worn off easily during sliding, exposing the bare metal surfaces to oxygen dissolved in the lubricant. This explains the formation of Al_2O_3 on the Al 6061 surface observed in Figs 8 and 9. The fragments of detached phosphate film act as obstacles to sliding and increase friction between the metal surfaces and the wear rate.

In this model, the high friction and low wear rate observed for L4-APi compared to L3-APa can be explained by assuming that L3-APa requires a higher TRA. If this is true, our testing conditions may not have been favorable for significant release of active phosphorus in L3-APa because its TRA was not reached as quickly as it was reached for L4-APi. In this case, the retained non-reacted phosphorus in L3-APa prevents oil oxidation during the initial stages of sliding. Consequently, no significant formation of Al_2O_3 will occur and the bare Al 6061 surface will be exposed to wear. Once the TRA is reached, of course, the same reaction mechanism as in L4-APi is expected to occur. The requirement of the temperature reaching the TRA of the respective lubricant additive also explains why the friction and wear we observed for L3-APa and L4-APi are higher than those observed for L2-SOf and L7-FFO. A quantitative verification of this hypothesis may be accomplished with the help of thermodynamic and mechanical data for iron- and aluminum phosphates.

6.3. Lubricant with ZDP

ZDPs are widely used lubricant additives for enhancing wear resistance. Their effectiveness is confirmed in our experiments, in which L6-ZDP showed the best anti-wear performance among all considered lubricants.

In accordance with results presented in the literature [25, 29], the performance of ZDP in L7-FFO is enhanced by forming a film composed of sulfur and phosphorus compounds that separates the counteracting surfaces. Initially, while the temperature is still low, ZDP is reversibly adsorbed on the metal surfaces. As the mechanical surface rubbing and the temperature increase, ZDDP components of the ZDP decompose into zinc dialkyl-phosphoryl-disulfide. This disulfide is adsorbed on the metal surfaces as well [30]. With the Fe in the AISI E 52100, the disulfide reacts to FeS. As explained for L2-SOf, FeS is mechanically soft [30]. The phosphate from the phosphoryl group reacts with both Al 6061 and AISI E 52100 to produce an amorphous layer of short-chain ortho- and meta-phosphates. This layer, which also incorporates sulfur, is best described as a phosphate "glass," in which Zn and Fe cations stabilize the amorphous structure. This layer is brittle. Therefore, similar to what we considered for phosphorus additives, the phosphate glass layer is easily erased during sliding, exposing the bare surface of Al 6061 to oxygen dissolved in the lubricant and/or from the ambient. Again, this causes oxidation of Al to Al_2O_3 at the Al 6061 surface, as observed in Fig. 10.

Interestingly, Fig. 10 features significant Zn and sulfur signals only within the first 5 nm of depth, but a strong oxygen signal over the entire depth range down to 100 nm. This can be explained as follows: Decomposition of ZDP continuously deposits ZnS (zinc sulfide) onto the surface. However, since ZnS only adheres poorly and is mechanically weak, it is continuously being replaced by oxide. The film formed on AISI E 52100 by the combined interaction of sulfur, phosphorus, and Zn leaves the AISI E 52100 side of the tribo-pair soft compared to the Al 6061 side, where a layer of Al_2O_3 forms. This reduces the wear rate of Al 6061. Consequently, ZDP provides the best wear resistance of all single additives we have tested in this study. Further work is required to understand why the combined effect of sulfur and phosphorus provides the Al 6061 surface with a better wear resistance than either sulfur or phosphorus alone (as observed for L2-SOf, L3-APa, L4-APi). The role of Si-rich precipitates and the formation of ZDDP tribo-

films on the steel counterpart has recently been studied by Shimizu and Spikes [31].

6.4. Ca detergent

The lubricant L5-OCS, based on Ca detergents, showed the highest friction coefficient on Al 6061 among all tested lubricants – and a rather high wear volume. The underlying micromechanism can be understood as follows: On mechanical interaction with the tribo-pair surfaces, the inverse $CaCO_3$ micelles with sulfonate head group and hydrocarbon tail that are present in L5-OCS become compacted and decompose to produce $CaCO_3$ and sulfonate groups [32, 33]. Subsequently, the $CaCO_3$ decomposes into CaO (calcium oxide) and CO_2. In this way, a layer of CaO forms on the metal surfaces, and a layer of $CaCO_3$ will be on top of it. As sliding progresses, the decomposition of $CaCO_3$ into CaO also continues. This formation mechanism of the Ca- and oxygen-rich layer on the Al 6061 surface observed in Fig. 11. Regarding the wear behavior of L5-OCS, the presence of an (1 – 3 nm thick) $CaCO_3$ layer on top of CaO has been observed to provide some wear resistance by itself [32, 33]. In our study, however, it showed the highest wear volume loss on the Al 6061 ball and the highest friction coefficients as well. This can be rationalized considering the brittleness of CaO and the lack of bonding between CaO and either of counter-face materials. The CaO will thus just physically embed into the Al 6061 surface. As sliding progresses, this CaO may form abrasive particles or wear debris that promote friction and wear. A quantitative verification of this hypothesis should be possible based on experimental data on the mechanical properties of CaO and its adhesion to Al 6061 and AISI E 52100.

6.5. Fully formulated lubricant

Based on the understanding of individual lubricant additives developed in the previous sections, we now attempt to explain the combined effect of ZDP and Ca detergents on friction and wear resistance of Al 6061 in L7-FFO, the fully formulated oil:

As sliding continues and the temperature increases to perhaps 450 to 480 K (150 to 180 °C) at the contact, the Ca detergents increasingly interact with ZDP. This results in a decrease of the ZDP decomposition rate [32, 33], reducing the rate at which ZDP deposits the protecting surface film onto Al 6061. At the same time, the Al 6061 surface may react with oxygen dissolved in the lubricant or originating from $CaCO_3$. Ergo, the decomposition products of ZDP and Ca detergents compete to react with the Al 6061 surface. This explains why in L7-FFO, Ca does not penetrate as deep as in L5-OCS alone. The competition of ZDP and Ca detergents for the Al 6061 surface also explains why the AES elemental maps in Fig. 14 show such a strong correlation between the spatial distributions of Al, oxygen, and Ca and a correspondingly strong anti-correlation with the spatial distributions of Zn and sulfur. Further, during the sliding process, the Ca detergents may modify the ZDP-derived anti-wear film by co-adsorbing on the surface [32, 33]. Possibly it is for this reason that the spatial distributions of Ca, Zn, and sulfur show good correlation in Fig. 14. The correlation between the spatial distributions of Fe, sulfur, and Zn with those of Al and oxygen on the Al 6061 wear scar can be understood as a soft Fe–S–Zn compound adhering to the hard aluminum oxide [32, 33]. Again, as the Ca detergents modify ZDP, the wear volume loss of Al 6061 in L7-FFO approximately corresponds to the average of the volume losses observed for L6-ZDP and L5-OCS alone.

6.6. Microstructure

The microcharacterization of Al tested with L7-FFO provides an enlightening example of the me-chanical damage that sliding induces in alloy surfaces even in (or because of) the presence of a lubricant. Most notable is the formation of small grains elongated in the sliding direction in a zone reaching down to a few hundred nanometers below the alloy surface. This reorganization of the grain structure can be understood as dynamic recrystallization [1]: In highly strained crystal regions, dislocations in Al are known to reorganize into a subgrain structure. If subgrains can form with crystal lattice orientations sufficiently different from those in their environment, they can develop mobile grain boundaries and act as nuclei for recrystallization – in this case dynami-cally, i. e. during deformation [34]. The observed grain structure and its explanation by dynamic recrystallization suggests that even in the presence of L7-FFO, the near-surface region of the alloy experiences high strain. In fact, the grain structure observed is very similar to what Terada et al. observed in Al 6061 after "severe" plastic deformation [35]. It seems possible that ongoing severe plastic deformation eventually leads to super-plastic behavior, enabled by grain boundary sliding and gliding of entire grains [36]. These mechanisms are known to promote elongated grains at the interface in the direction of sliding and are relatively thin resembling layers of flat "tiles" [1]. Under static conditions, on the other hand, the Hall–Petch relationship predicts increased hardness of the zone with refined grain size.

In addition to the structural modification, sliding induces changes in the surface composition. Ac-cording to the results of the XEDS analysis, additional phases can be deposited on the surface of the Al alloy by transfer of material from the sliding counterpart, i. e. steel, as well as by reaction with components of the lubricant. Regarding the latter, CaO with rocksalt structure constitutes the main deposit originating from L7-FFO. Formation of CaO can be explained by decomposition Ca-containing detergents present in L7-FFO, as discussed earlier. The presence of small particles of Fe in the CaO is expected to be the Fe wear debris that is embedded into CaO during sliding. This can be expected from the adhesion of Fe from the steel counterpart to the aluminum oxide that forms during sliding, as discussed above. According to work of Tarasov et al., it would be expected that the main deposit of steel debris occurs on the trailing hemisphere of the Al ball [37].

7. Conclusions

The results of the present study lead to the following conclusions:

1. Just adding SOf (sulfurized olefin) to MBO (group II mineral base oil) effectively reduces friction and wear between Al 6061 and AISI E 52100. On Al 6061, this additive deposits hardly any sulfide. Apparently, the

low friction and wear originate from combined formation of Al_2O_3 on the Al alloy and FeS on the steel, both reducing adhesion by preventing direct metal–metal contact.

2. Compared to FFO (fully formulated oil API SN 5W-30), MBO with APa (complex alkyl phos-phate amine) or APi (alkyl phosphite) as the only additive, both providing phosphorus, causes high friction and wear. Similar to SOf (sulfurized olefin), these additives also produce Al_2O_3 on the Al alloy, but no anti-wear films of phosphate or phosphite.
3. Secondary ZDP (zinc dithiophosphate) most effectively reduces the wear on Al 6061 among the lubricants studied here. Different from the conclusions drawn in earlier studies, however, this additive neither causes significant phosphate nor sulfide formation on Al 6061. Like SOf, APi, and APa, ZDP mostly produces Al_2O_3 on the Al alloy surface. This suggests that the observed reduction of wear actually originates from a $ZnPO_4$ layer that forms on the *steel*.
4. The friction and wear in MBO with the sole addition of OCS (overbased Ca sulphonate detergent) are higher than in FFO (fully formulated oil API SN 5W-30). While the wear rate is not too much higher than in FFO, the friction coefficient is as high as that of MBO with just ZDP. This agrees with literature proposing the formation of Ca carbonate pads – thicker than 100 nm and similar to the phosphate pads formed by ZDP. Remarkably, OCS (overbased Ca sulphonate detergent) is the only additive in this study that does not promote the formation of Al_2O_3 on Al 6061.
5. The wear volume loss of Al 6061 in FFO corresponds to the average observed for MBO with just ZDP and MBO with just OCS. This can be understood from ZDP and OCS both forming protective pads that prevent direct metal–metal contact. The lower friction compared to MBO with just one of these additives likely results from other additives in the FFO, such as "friction modifiers" that physisorb but not chemisorb on the Al alloy surface.
6. Even in the presence of L7-FFO lubricant, the tribotested Al alloy undergoes severe plastic deformation within a zone from the surface to a depth of several hundreds of nanometers.
7. This highly plastically deformed region developed small grains that are elongated in the sliding direction. This can be explained by dynamic recrystallization.
8. Interaction with the L7-FFO lubricant generates a tribofilm with a high concentration of CaO nanocrystals with the rocksalt structure.
9. The mechanical interaction with the steel counterpart causes Fe nanoparticles to be incorporated into the CaO tribo-film.

We acknowledge fruitful discussion with AH Heuer, J Lewandowski, and R Sharghi-Moshtaghin. This work was supported by the Ohio Department of Development under Agreement Number of TECH 09-012.

References

[1] G. Stachowiak, A.W. Batchelor (Eds.): Engineering Tribology: volume 24 of Tribology Series: Elsevier, Amsterdam: 2005.
[2] E. Rabinowicz: Friction and Wear of Materials: Wiley, New York: 1965.
[3] P. Kumar, M.F. Wani: Jurnal Tribologi 15 (2017) 21–49.
[4] N.M. Rusin, A.L. Skorentsev, E.A. Kolubaev: J. Frict. Wear 37 (2016) 86–93. DOI:10.3103/S1068366616010141
[5] R.E. Winter, S.M. Stirk, G.J. Ball, L.S. Markland: Journal of Physics D –Applied Physics 47 (2014). DOI:10.1088/0022-3727/47/4/045501
[6] F. Jian-hua, P. Fu-sheng, C. Bo-shui, W. Jiang, D. Ling: Transactions of Nonferrous Metals Society of China 21 (2011) 2649–2653. DOI:10.1016/S1003-6326(11)61105-9
[7] F. Nan, Y. Xu, B. Xu, F. Gao, Y. Wu, X. Tang: Appl. Surf. Sci. 307 (2014) 86–91. DOI:10.1016/j.apsusc.2014.03.170
[8] H. Wu, J. Zhao, X. Cheng, W. Xia, A. He, J.H. Yun, S. Huang, L. Wang, H. Huang, S. Jiao, Z. Jiang: Tribol. Int. (2018) 24–38. DOI:10.1016/j.triboint.2017.08.011
[9] M.A. Nicholls, P.R. Norton, G.M. Bancroft, M. Kasrai: Wear (2004) 311–328. DOI:10.1016/j.wear.2003.12.007
[10] J. Fang, B. Chen, W. Liu, L. Dong, J. Wang: Transactions of Nonferrous Metals Society of China 14 (2004) 435–438. 4th International Conference on Surf. Eng., Shenzhen, Peoples R China, OCT 29–31, 2004. PMid:15096554
[11] P. Faverjon, J. Rech, R. Leroy: J. Tribol. – Transactions of the ASME 135 (2013). DOI:10.1115/1.4024546
[12] R. Liu, D. Li: J. Mater. Sci. 35 (2000) 633–641. DOI:10.1023/A:1004780528202
[13] Z. Mu, F. Zhou, S. Zhang, Y. Liang, W. Liu: Tribol. Int. 38 (2005) 725–731. DOI:10.1016/j.triboint.2004.10.003
[14] S. Tseregounis: Tribol. Trans. 39 (1996) 1–12. DOI:10.1080/10402009608983496
[15] Y. Wan, Q. Xue: Tribol. Lett. 2 (1996) 37–45. DOI:10.1007/BF00182546
[16] Y. Wan, W. Liu, Q. Xue: Wear 193 (1996) 99–104. DOI:10.1016/0043-1648(95)06680-2
[17] Z. Karim, M.Z. Nuawi, J.A. Ghani, M.J. Ghazali, S. Abdullah, N.I.I. Mansor: Wear 334 (2015) 99–104. DOI:10.1016/j.wear.2014.11.012
[18] H. Spikes: Tribol. Lett. 60 (2015) 1–26. DOI:10.1007/s11249-015-0589-z
[19] G. Pereira: Tribology 1 (2007) 48–62. DOI:10.1179/175158407X189293
[20] C. Chen, H. Bosse, L. Deters: Engineering Tribology 223 (2009) 571–582. DOI:10.1243/13506501JET511
[21] J. Walker, I. Ross, W. Rainforth, M. Lieblich: Wear 263 (2007) 707–718. DOI:10.1016/j.wear.2006.12.043
[22] M.I.D.B. Bouchet, J.M. Martin, C. Oumahi, O. Gorbatchev, P. Afanasiev, C. Geantet, R. Iovine, B. Thiebaut, C. Heau: Tribol. Int. 119 (2018) 600–607. DOI:10.1016/j.triboint.2017.11.039
[23] G. Pereira: Tribology (2007) 105–113. DOI:10.1179/175158407X231303
[24] ASTM, ASTM G99-05 (2010) standard test method for wear testing with a pin-on-disk apparatus, 2012.
[25] Y. Wan, Q. Xue: Wear 188 (1995) 27–32. DOI:10.1016/0043-1648(94)06589-6
[26] A.H. Heuer, D.B. Hovis: J. Microsc. 240 (2010) 173–180. PMid:21077878; DOI:10.1111/j.1365-2818.2010.03399.x
[27] S. Lingala, Microstructural Characterization of an Aluminum Alloy Tribo-Tested Against Steel in The Presence of Lubricants, Master's thesis, Case Western Reserve University, 2011.
[28] D.R. Lide (Ed.): CRC Hand book of Physical and Chemical Data: CRC Press LLC, Boca Raton, Florida, USA: 88 edition: 2007–2008.
[29] R. Schumacher, H. Zinke: Tribol. Int. 30 (1997) 199–208. DOI:10.1016/S0301-679X(96)00043-6
[30] L.R. Rudnick: Lubricant Additives: Chemistry & Applications: Chemical Industries Series: CRC Press, Boca Raton, Florida, USA: 2 edition: 2008.
[31] Y. Shimizu, H.A. Spikes: Tribol. Lett. 65 (2017) 1–13. DOI:10.1007/s11249-017-0915-8
[32] M.T. Costello: Tribol. Trans. 49 (2006) 592–597. DOI:10.1080/10402000600927563
[33] M. Kasrai, M.S. Fuller, G.M. Bancroft, P.R. Ryason: Tribol. Trans. 46 (2003) 534–542. DOI:10.1080/10402000308982660
[34] A. Berger, P.J. Wilbrandt, F. Ernst, U. Klement, P. Haasen: Progress in Mater. Sci. 32 (1988) 1–95. DOI:10.1016/0079-6425(88)90009-6

[35] D. Terada, Y. Kaneda, Z. Horita, K. Matsuda, S. Hirosawa, N. Tsuji: IOP Conference Series: Materials Science and Engineering 63 (2014) 012088-1-5. DOI:10.1088/1757-899X/63/1/012088
[36] E. Esquivel, L. Murr: Mater. Sci. Eng. A 409 (2005) 13 – 23. DOI:10.1016/j.msea.2005.04.063
[37] S.Y. Tarasov, A.V. Filippov, E.A. Kolubaev, T.A. Kalashnikova: Tribol. Int. 115 (2017) 191 – 198. DOI:10.1016/j.triboint.2017.05.039

(Received January 10, 2018; accepted March 26, 2018; online since July 9, 2018)

Correspondence address

Frank Ernst
Department of Materials Science and Engineering
Case School of Engineering, CWRU
Cleveland, OH 44106-7204
USA
E-mail: fxe5@case.edu

Bibliography
DOI 10.3139/146.111673
Int. J. Mater. Res. (formerly Z. Metallkd.)
109 (2018) 9; page 789 – 802

ISSN 1862-5282